inorganics

MDPI

Article

High-Throughput Synthesis of Pillared-Layered Magnesium Tetraphosphonate Coordination Polymers: Framework Interconversions and Proton Conductivity Studies

Rosario M.P. Colodrero [1], Inés R. Salcedo [2], Montse Bazaga-García [2], Eleni Barouda [3], Maria Papadaki [3], Konstantinos E. Papathanasiou [3], Daniel Hernández-Alonso [2], Jordi Rius [4], Miguel A.G. Aranda [5], Enrique R. Losilla [2], Pascual Olivera-Pastor [2], Konstantinos D. Demadis [3,*] and Aurelio Cabeza [2,*]

1 Faculty of Science & Engineering, University of Wolverhampton, Wulfruna Street, Wolverhamton WV1 1LY, UK; r.perezcolodrero@wlv.ac.uk
2 Departamento de Química Inorgánica, Universidad de Málaga, Campus Teatinos s/n, 29071 Málaga, Spain; inesrs@uma.es (I.R.S.); m.bazaga@uma.es (M.B.-G.); hernandez.alonso.d@gmail.com (D.H.-A.); r_losilla@uma.es (E.R.L.); poliverap@uma.es (P.O.-P.)
3 Crystal Engineering, Growth and Design Laboratory, Department of Chemistry, University of Crete, Voutes Campus, Crete GR-71003, Greece; leni_mpar@yahoo.gr (E.B.); magia@chemistry.uoc.gr (M.P.); kpapatha@fiu.edu (K.E.P.)
4 Institut de Ciència de Materials de Barcelona (CSIC), 08193 Bellaterra, Catalunya, Spain; jordi.rius@icmab.es
5 ALBA Synchrotron, Ctra. BP1413 km 3.3, 08290 Cerdanyola del Vallès, Barcelona, Spain; g.aranda@cells.es
* Correspondence: demadis@uoc.gr (K.D.D.); aurelio@uma.es (A.C.); Tel.: +30-2810-545051 (K.D.D.); +34-952-131-874 (A.C.)

Received: 8 August 2018; Accepted: 7 September 2018; Published: 11 September 2018

Abstract: Novel pillared-layered framework materials were synthesized by high-throughput or microwave-assisted methodology that contain Mg^{2+} and the zwitterionic linker HDTMP (hexamethylenediamine-*N,N,N′,N′-tetrakis*(methylenephosphonic acid)). Three compounds were structurally characterized by X-ray powder diffraction. In the compound $\{Mg[(HO_3PCH_2)_2N(CH_2)_6N(CH_2PO_3H_2)_2]\cdot(H_2O)\}_n$(**1**), obtained at 140 °C by hydrothermal or microwave-assisted reaction, the layers are built by isolated Mg^{2+} octahedra coordinated by oxygen atoms from six different zwitterionic HDTMP ligands. Each amino-*bis*(methylenephosphonate) moiety links three Mg^{2+} ions, bridging two of them through one phosphonate group and connecting the third polyhedron in a monodentate fashion. In Compound **2**, $\{Mg[(HO_3PCH_2)_2N(CH_2)_6N(CH_2PO_3H_2)_2]\}_n$, hydrothermally synthesized at 180 °C, the layers are composed of bidentate amino-*bis*(methylenephosphonate) moieties connected to three Mg^{2+} ions, with one of the phosphonate groups acting as a bridging ligand. Various subtle structural changes are noted for the other two compounds. Thermodiffraction of **1** reveals that a crystalline-to-crystalline phase transformation occurs concomitantly with its dehydration, leading to a new anhydrous phase, namely, $\{Mg[(HO_3PCH_2)_2N(CH_2)_6N(CH_2PO_3H_2)_2]\}_n$**(1deh)**. This process is fully reversible upon equilibrating the solid at room temperature. The reported compounds can adsorb ammonia and CO_2. Compound **1** exhibits a moderate proton conductivity, ~1.5×10^{-5} S·cm^{-1} at 80 °C and 95% RH, that increases a half order of magnitude after experiencing a complete dehydration/rehydration process, **1**→**1deh**→**1**.

Keywords: proton conductivity; coordination polymers; metal phosphonates; tetraphosphonates; gas adsorption; dehydration/rehydration

1. Introduction

Among the large family of (poly)phosphonate ligands [1], those that contain an amino group constitute a special category. The so-called aminomethylenephosphonates are prepared from a primary amine via the "Mannich-type" reaction (also referred to as the "Irani-Moedritzer" reaction) [2]. Some of their attractive structural features include (a) variation in the number of phosphonate groups, based on the number of starting amine groups (e.g., one primary amine can be converted to two methylenephosphonate moieties), (b) flexibility of the polymethylene chain connecting the N atoms, (c) structural systematics in the case of systematically altered starting amines, and (d) the zwitterionic character of the molecule (the basic N atom is always protonated at pH < 10) [3].

A particular group of tetraphosphonates (see Figure 1) has been synthesized starting from the corresponding diamines [4]. In these, the N atoms are linked with a systematically elongated polymethylene chain (from two to twelve carbon atoms), whereas the two ends of the molecule are the same, with an amino-*bis*(methylenephosphonate) on each side.

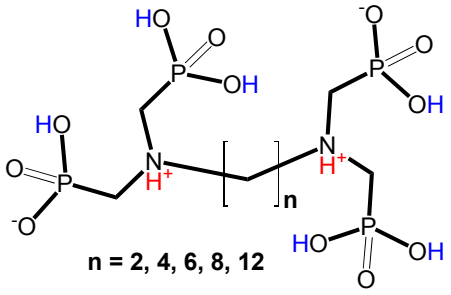

Figure 1. Generic structure of the tetraphosphonate ligands in the neutral, zwitterionic form.

Various members of this family have been used for several applications. A complex of ^{153}Sm with EDTMP (n = 2) has been investigated as a potential radiotherapeutic agent for treatment of bone tumors [5]. Hybrid materials of EDTMP and HDTMP (n = 6) with various alkaline-earth metal ions have been used as metallic corrosion inhibitors [6,7]. Coordination polymers with HDTMP have shown gas uptake properties, including a breathing behavior and NH_3 adsorption [8,9]. Furthermore, the 3D La-HDTMP showed high proton conductivity, up to 8×10^{-3} S·cm^{-1}, and NO releasing capabilities [10]. Photoluminescent lanthanide-HDTMP materials "decorated" with sulfate anions have been also recently reported. The latter materials were demonstrated to be amenable to synthetic modification by inclusion of auxiliary anions, such as sulfate [11]. By increasing the alkyl chain length of the ligand to n = 8 (ODTMP) led to an 3D ultramicroporous structure (Mg-ODTMP) exhibiting high CO_2 selectivity from CO_2/CH_4 mixtures and proton conductivity (1.6×10^{-3} S·cm^{-1}) [12].

In addition to the aforementioned "flexible" aminomethylene tetraphosphonate linkers, there is a plethora of other rigid ligands. A few examples are warranted. Tetraphosphonates and their corresponding metal derivatives, based on "flat" phenyl and anthracene cores, have been reported. [13]. Phenyl groups-containing compounds exhibited proton conductivity properties which specifically depend on the relative position of the phosphonic groups [14,15]. With this type of rigid ligand, high catalytic and proton conductivities, up to 2.58×10^{-2} S·cm^{-1}, were found [16]. Tetraphosphonates with a tetrahedral structure have been also published [17,18]. Recently, a review on tetraphenylmethane (TPPM) and tetraphenylsilane (TPPSi) as building units of coordination polymers has been reported [19]. Other groups of materials derive from porphyrin cores with peripheral phosphonate [20]. The resulting isostructural porphyrin-based phosphonates showed high crystallinity, chemical stability, and permanent porosity. The reader is referred to a recent excellent review on various tetraphosphonate linker structural types and their metal derivatives [21].

In this paper, we describe the preparation, characterization, structural determination, and gas adsorption and proton conductivity properties of a family of three new magnesium tetraphosphonates—Mg-HDTMP (HDTMP = hexamethylenediamine- *N*,*N*,*N*′,*N*′-*tetrakis* (methylenephosphonic acid)), two of which are

polymorphs. The CO_2 and NH_3 uptake/desorption together with the induced structural changes in the frameworks of these Mg-HDTMPs are discussed. Additionally, the proton conductivity properties for the three magnesium compounds are reported and the influence of the dehydration/rehydration processes in enhancing the proton conductivity values is underlined.

2. Results and Discussion

The hydrothermal synthesis screening revealed that the compound $\{Mg[(HO_3PCH_2)_2N(CH_2)_6N(CH_2PO_3H_2)_2]\cdot(H_2O)\}_n$**(1)** was the only monophasic product that could be isolated from aqueous solution, with a Mg:HDTMP molar ratio 1:2 and pH < 1.5. In contrast, other synthetic conditions led to mixed phases. Furthermore, the title compound was obtained by MW-assisted synthesis much more rapidly (30 min vs. 7 days), at the same experimental conditions and with higher yields (see Experimental Section). Synthesis of the compound $\{Mg[(HO_3PCH_2)_2N(CH_2)_6N(CH_2PO_3H_2)_2]\}_n$ (**2**) required a Mg:HDTMP molar ratio 1:1, pH = 2.3, and a reaction conducted at 180 °C (5 days) in aqueous solution or at 130 °C in mixed H_2O/DMF = 1:2 v/v or with a H_2O/DMF molar ratio = 1:4, with at least a metal/ligand molar ratio of 1:4. It was noted that this compound appears as a minority secondary phase in most solids isolated from reactions run at 130 °C in aqueous solutions.

2.1. Thermal Behavior

The TG curve for **1** reveals a one step-dehydration taking place in the 135–180 °C range with an associated weight loss of 3.79%, which is consistent with the loss of one water molecule (calculated 3.38%), compared to the anhydrous solid **2** (Figure 2). Ligand decomposition starts above 320 °C.

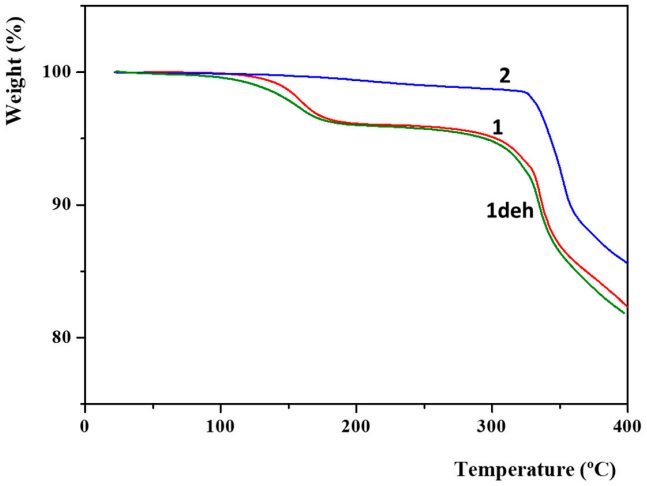

Figure 2. Thermal analysis for Compounds **1**, **2**, and **1deh** after rehydration.

Further studies by thermodiffraction of Compound **1** (Figure 3) indicate that the solid remains crystalline before decomposition and, moreover, a crystalline-to-crystalline phase transformation occurs concomitantly with its dehydration, leading to a new anhydrous phase, namely, $\{Mg[(HO_3PCH_2)_2N(CH_2)_6N(CH_2PO_3H_2)_2]\}_n$(**1deh**). This process is fully reversible upon equilibrating the solid at room temperature.

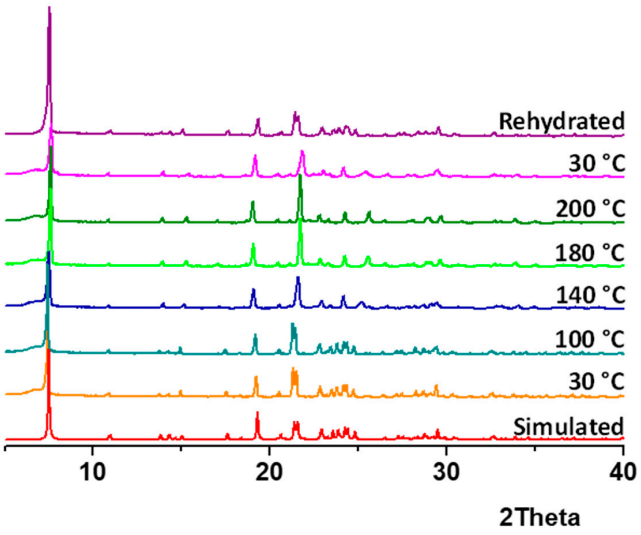

Figure 3. X-ray diffraction patterns of Solid **1** at different temperatures and after rehydration.

2.2. Crystal Structures

Crystal structures for Compounds **1** and **2** were solved ab initio from laboratory X-ray powder diffraction data, while Compound **1deh** was solved by Rietveld refinement using as a starting structural model the crystal structure reported for Mg-ODTMP·$2H_2O$ (ODTMP stands for the octamethylene analog of HDTMP) [12]. Crystallographic data for all studied compounds are presented in Table 1, and the final Rietveld plots are given in Figures S1–S3 (Supplementary Materials).

Table 1. Selected crystallographic data for magnesium tetraphosphonate materials from laboratory powder X-ray diffraction.

Compound	1	1deh	2
Chemical formula	$MgP_4O_{13}N_2C_{10}H_{28}$	$MgP_4O_{12}N_2C_{10}H_{26}$	$MgP_4O_{12}N_2C_{10}H_{26}$
Formula Mass	532.54	514.52	514.52
Crystal system	Triclinic	Monoclinic	Triclinic
Space Group	$P\bar{1}$	$C2/c$	$P\bar{1}$
λ/Å	1.5406	1.5406	1.5406
a/Å	12.5276(3)	23.469(1)	12.362(2)
b/Å	9.70223(2)	8.6872(4)	9.0720(1)
c/Å	8.62223(2)	9.6165(5)	9.552501)
α/°	91.917(1)	90.0	90.6651(8)
β/°	70.621(1)	99.219(4)	106.7290(9)
γ/°	86.485(2)	90.0	111.8975(8)
Unit cell volume/Å^3	985.16(4)	1935.3(2)	943.45(2)
Z	2	4	2
$V_{\text{non-H-atom}}$/Å^3	16.42	16.68	16.27
Temperature/K	298	493	298
No. independent reflections	2043	588	1947
Data/Restrains/Parameters	5710/65/132	4147/33/75	5398/63/135
R_{WP}	0.0474	0.0812	0.0617
R_P	0.0361	0.0602	0.0482
R_F	0.0654	0.0500	0.0425
CCDC number	1855415	1855416	1855417

Compounds **1** and **2** crystallize in the triclinic system. Both contain two Mg^{2+} ions in special positions, and a crystallographically independent $HDTMP^{2-}$ ligand. Compound **1deh**, isoreticular with Mg-ODTMP·$2H_2O$ [12], crystallizes in the monoclinic system with space group $C2/c$. All solids exhibit pillared layered structures. For Compounds **1** and **1deh**, the layers (plane *bc*) are built by isolated Mg^{2+} octahedra coordinated by oxygen atoms from six different zwitterionic HDTMP ligands [22–27]. Each amino-*bis*(methylenephosphonate) moiety links three Mg^{2+} ions, bridging two of them through one phosphonate group and connecting the third polyhedron in a monodentate fashion. The two free oxygens of the monodentate phosphonate group point toward the interlayer space (Figure 4). Each layer in Compound **2** is constructed by bidentate amino-*bis*(methylenephosphonate) moieties connecting three Mg^{2+} ions, while one of phosphonate groups acts as a bridging ligand (Figure 4). Again, the two uncoordinated oxygens of the other phosphonate group point toward the interlayer space. For all three structures, neighboring layers are propped apart along the *c* axis by the alkyl chain (Figure 5). Viewed along the *b* axis, 1D channels result in the interlayer region of **1** and **1deh** frameworks, which are filled by the lattice water in **1.** Consequently, H-bonding interactions arise between the water and the hydrogenphosphonate groups (Figure S4 and Table S1), which are absent when no water is present, as in Compound **1deh** (Table S2). However, the different metal/ligand connectivity displayed in Compound **2** demonstrates strong H-bonding interactions between proximal, "face-to-face" hydrogenphosphonate groups located in interlayer hydrophilic channels (Table S3).

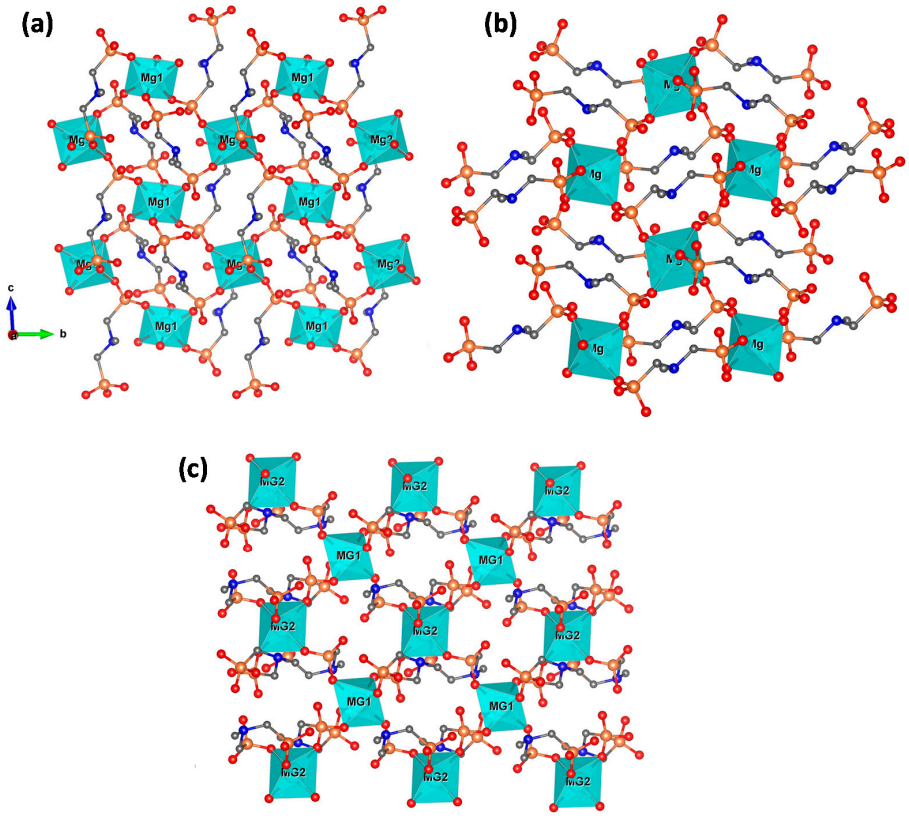

Figure 4. Representation of the layers for Compounds **1** (**a**), **1deh** (**b**), and **2** (**c**) [28].

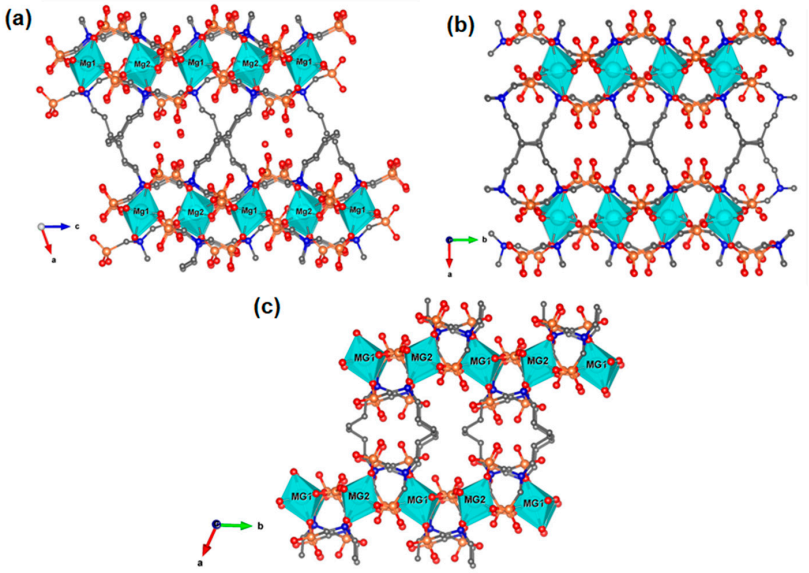

Figure 5. View of the 3-D packing for Compounds **1** (**a**), **1deh** (**b**), and **2** (**c**) [28].

2.3. Gas Adsorption

N_2 and CO_2 adsorption isotherms were measured for degassed Compounds **1** and **2** (see Figure S5 as an example). N_2 adsorption are typical of non-porous solids (BET surface area of $\leq$4 $m^2 \cdot g^{-1}$). On the other hand, CO_2 adsorption collected at 273 K and under pressure up to 1 bar, gave surface areas, as deduced from the Dubinin–Radushkevich equation, of 55 $m^2 \cdot g^{-1}$ and 11 $m^2 \cdot g^{-1}$, corresponding to total amounts of adsorbed CO_2 of 0.105 and 0.05 $mmol \cdot g^{-1}$, respectively. The obtained CO_2 adsorption capacities are significantly lower than that obtained for Mg-ODTMP (0.8 mmol/g). This behavior can be attributed to the higher flexibility imparted by a longer linker (8 vs. 6 carbon atoms) in order to accommodate weakly adsorbed guest molecules, such as CO_2. At high CO_2 pressures (3–10.5 bar), Compound **1deh** (obtained by in situ dehydration of **1** at 200 °C under CO_2 flow and pressure 3 bar) behaves as a guest-responsive framework as revealed by the splitting of low angle diffraction peaks that may be attributed to different conformations of the pillaring alkyl chains occurring upon CO_2 degassing from 10.5 to 1 bar (Figure 6). Concomitant to this crystalline-to-crystalline transformation, a partial amorphization was also detected. All these changes became permanent upon completion the adsorption/desorption process.

Exposure of Solids **1** and **2** to concentrated ammonia solution (14%) led to two new partially amorphized phases, **3** and **4**, respectively, with different water/ammonia content, but without any structural changes in the crystalline phases. The reaction with ammonia occurs via a different process in Compounds **1** and **2**. While the particle sizes for **1** and **3** are quite similar, ~1200 and 1400 Å, respectively, the adsorption of ammonia by Solid **2** provokes a significant reduction in the particle sizes, from 1190 Å, for Solid **2,** to 758 Å for **4**. This fact suggests a distinct hydrolytic mechanism that is corroborated by the higher uptake of guest species (NH_3/H_2O) observed for **4** than for **3** (9.5 NH_3/H_2O molecules vs. 5.5 molecules per formula for **4** and **3**, respectively).

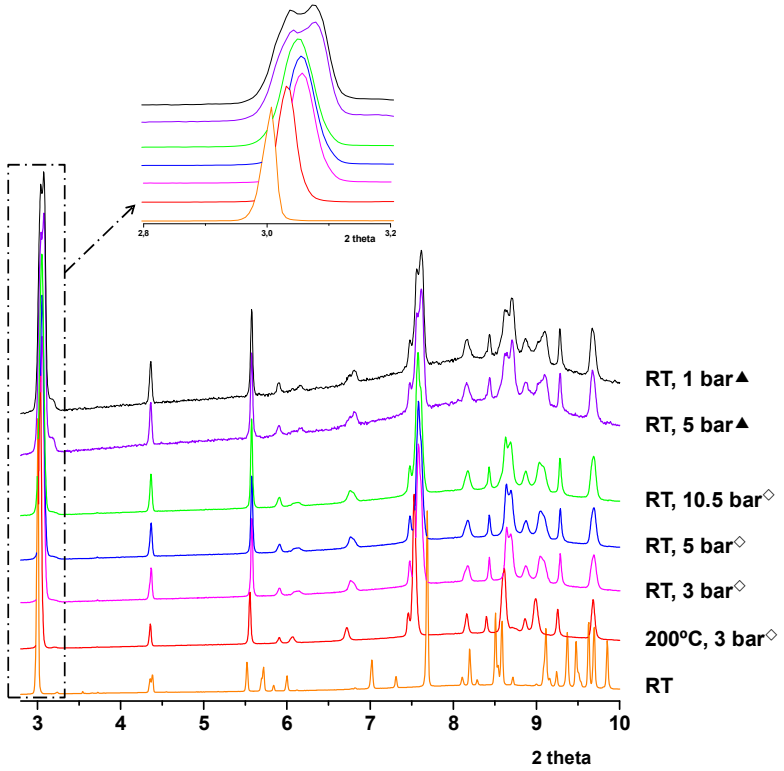

Figure 6. Synchrotron X-ray powder diffraction patterns for Compound **1** at different CO_2 pressures. Inset: splitting of diffraction peaks upon CO_2 adsorption (◇)/desorption (▲).

2.4. Proton Conductivity

Based on the H-bonding interactions observed in the three compounds, *ac* impedance measurements were carried out on powdered samples in the temperature range 30–80 °C, and at two humidity values, 75% and 95% RH, in order to probe potential proton conductivity behavior. The proton conductivity study was carried out for all compounds except for the ammonia-containing products, which were highly hygroscopic materials and, therefore, their proton conductivity properties could not be reliably determined. The total pellet resistance (RT) were obtained from the intercept of the spike and/or the arc on the Z′ axis from the Nyquist plots (Figures S6–S8). The overall pellet conductivities for all compounds are given in Figure 7, in traditional Arrhenius format. As can be observed, both Solids **1** and **2** exhibit quite similar proton conductivity values, ~1.5×10^{-5} S·cm^{-1} at 80 °C and 95% RH. These values are highly humidity-dependent and dropped to 6.5×10^{-7} S·cm^{-1} and 4.5×10^{-7} S·cm^{-1} at 75% RH and 80 °C for Compounds **1** and **2**, respectively. According to their post-impedance TG curves (not shown) and powder X-ray diffractions (Figures S9 and S10), these compounds demonstrated neither water uptake, nor structural changes during the proton conductivity measurements. In contrast, Compound **1deh** rehydrates reversibly to yield Compound **1** during the equilibration time at 80 °C and 95% RH, before the proton conductivity measurements. Interestingly, the resulting rehydrated solid exhibits a higher proton conductivity value, 6.6×10^{-5} S·cm^{-1} at 80 °C and 95% RH, a half order of magnitude higher than for the "as synthetized" compound. The powder X-ray diffraction pattern of the sample post-impedance, Figure S11, confirms the structural change and its rehydration and only minor variations in its TG curve (Figure 2) are observed. Although the rehydrated compound shows the same water content as **1**, the loss of lattice water starts at lower temperature, ~95 °C, suggesting changes in the H-bonding interactions between the lattice water and the framework after rehydration. These subtle modifications may provoke variations in the acidity of phosphonic acid groups, which point toward the 1D channels, as well as in the water mobility, what could justify the proton conductivity enhancement for the rehydrated sample. Hence,

the dehydration/rehydration processes may be envisioned as a pre-activation mechanism in order to increase the proton conductivity. On the other hand, the low activation energy values (<0.5 eV) indicated by the Arrhenius plot for all compounds (except for the rehydrated **1deh** at 75% RH) are in range for Grotthuss-mediated conduction [29]. For the rehydrated **1deh**, the activation energy increases up to 0.59 eV at 75% RH, which is consistent with a vehicle transport mechanism, and corroborates subtle structural modifications during the rehydration process of Compound **1deh**.

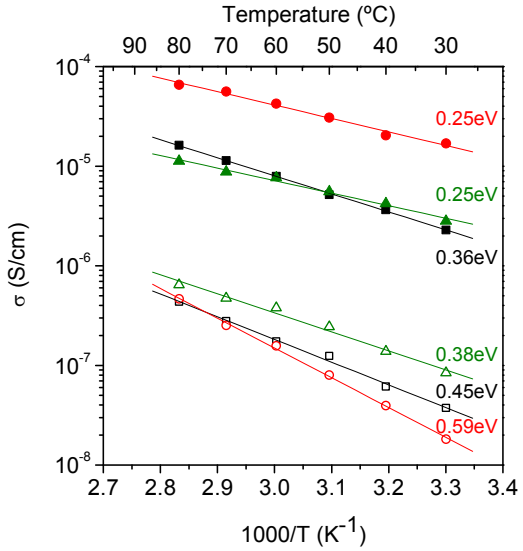

Figure 7. Arrhenius plots in the range between 30 and 80 °C at 75% (empty) and 95% RH (filled) for Compounds **1** (black), **1deh** (red), and **2** (green).

The moderate proton conductivity exhibit by the Mg-HDTMP compounds contrasts with the high proton conductivity values obtained for La-HDTMP·5H_2O [10] ($\sigma = 8 \times 10^{-3}$ S·cm^{-1} at 19 °C and 98% RH) or for the isoreticular derivative Mg-ODTMP·6H_2O ($\sigma = 1.6 \times 10^{-3}$ S·cm^{-1} at 19 °C and ~100% RH) [12], both of them showing similar pillared layered structures. It appears that the higher water content present in the channels of these materials, together with the longer alkyl chain in the Mg-ODTMP derivative induce more efficient H-bonding networks for the proton transfer processes, together with a higher structural flexibility.

3. Materials and Methods

3.1. General Information

All water-soluble metal salts were commercial samples and were used without further purification. HDTMP [hexamethylenediamine-*N*,*N*,*N*′,*N*′-*tetrakis*(methylenephosphonic acid)] was synthesized according to literature procedures [30] or was obtained commercially (as Dequest 2051 from ThermPhos-Dequest, Louvain-La-Neuve-Sud, Belgium). Stock solutions of HNO_3 or NH_3 (1 M, and 5 M) were used for pH adjustments. In-house, deionized (DI) water was used for all syntheses. Microwave-assisted hydrothermal syntheses were carried out in a microwave oven (Anton Paar GmbH–Monowave 300, Anton Paar GmbH, Graz, Austria). Elemental analyses (C, H, N) were measured on a Perkin-Elmer 240 analyzer. Thermogravimetric analysis (TGA) data were recorded on an SDT-Q600 analyzer from TA instruments (TA instruments, Barcelona, Spain). The temperature varied from RT to 900 °C at a heating rate of 10 °C·min^{-1}. Measurements were carried out on samples in open platinum crucibles under air-flow.

3.2. Small Scale-Synthesis: High-Throughput Study

Synthesis conditions were screened by high-throughput methodology with a system previously reported [31,32]. The aluminum autoclave block contains 36 Teflon-lined reaction chambers of 5 mL volume. Hydro/solvothermal reactions of HDTMP acid with Mg^{2+} salt were carried out in H_2O and DMF/H_2O mixtures (2:1 *v*/*v* and 4:1 molar) and different metal/ligand molar ratios. A total filling volume of ~3 mL per reactor was used. Routinely, the reaction block was heated to 130 °C for 3 days, except for one experiment that was run at 180 °C and a Mg:HDTMP molar ratio of 1:1 for 5 days in water. The reaction products were eventually filtered off, washed with water, and dried at 50 °C.

Hydrothermal reactions. The reaction mixture was prepared by mixing a 0.061 M aqueous solution of $Mg(NO_3)_2{\cdot}6H_2O$ with a 0.12 M aqueous solution of HDTMP acid (the ligand was dissolved by adding dropwise a 1 M aqueous solution of NH_3 to a suspension of the solid product in 10 mL of DI water up to a clear solution, pH = 2.5). For these syntheses, 1:1, 1:2, and 2:1 Mg:HDTMP molar ratios and initial pH values of 1.5, 2.5, 3.5, and 4.5 were tested. Other pH values tested were 0.5, 1.0, 4.0, 5.5, and 6.5 for Mg:HDTMP molar ratio 1:1 and 0.5 and 1.0 for Mg:HDTMP molar ratio 1:2.

Solvothermal reactions. In this case, DMF/H_2O mixtures were employed and MgO was used as the Mg^{2+} source, instead of $Mg(NO_3)_2{\cdot}6H_2O$. For the syntheses in DMF/H_2O (2:1 *v*/*v*), Mg:HDTMP molar ratios of 1:1, 1:2, and 2:1 were studied, whereas for 1:4 *v*/*v* H_2O/DMF Mg:HDTMP molar ratios of 1:1, 1.5:1 and 2:1 were tested.

3.3. Synthesis Scale-Up

Once the synthesis conditions were optimized by high-throughput screening, reactions were scaled up in order to obtain sufficient quantities of products for further characterization. $\{Mg[(HO_3PCH_2)_2N(CH_2)_6N(CH_2PO_3H_2)_2]{\cdot}(H_2O)\}_n$**(1)**.was prepared by dissolving $Mg(NO_3)_2{\cdot}6H_2O$ (0.305 mmol, 78.2 mg) in 5.0 mL of deionized water under stirring. Separately, 300 mg of solid HDTMP (0.609 mmol) was dissolved in 5 mL of deionized water by consecutive addition of 5 M and 1 M NH_3 solutions. The pH of this solution was ~2.5. The two solutions are mixed under vigorous stirring (the ligand solution was slowly dripped into the Mg-containing solution), and the final pH was modified to ~1. The reaction was conducted at 140 °C for 7 days in a Teflon-lined autoclave with a volume of 45 mL. The resulting solid was filtered off, washed twice with DI and acetone, and dried at 50 °C. Elemental analysis for $MgP_4O_{12}N_2C_{10}H_{26}{\cdot}H_2O$ **(1)**: calculated (wt %): C 22.55, H 5.30, N 5.26; found (wt %): C 22.25, H 5.30, N 5.29. Yield ~52% based on the metal.

The anhydrous phase, $\{Mg[(HO_3PCH_2)_2N(CH_2)_6N(CH_2PO_3H_2)_2]\}_n$ **(1deh)**, was obtained upon dehydration of **1** at 180 °C.

A new anhydrous phase, $\{Mg[(HO_3PCH_2)_2N(CH_2)_6N(CH_2PO_3H_2)_2]\}_n$ **(2)**, was prepared by dissolving $Mg(NO_3)_2{\cdot}6H_2O$ (0.609 mmol, 156.3 mg) in 12.0 mL of deionized water under stirring. Then, 300 mg (1.756 mmol) of HDTMP were added to it as a solid. The pH was modified to 2.1 until everything dissolves. The reaction was heated at 180 °C for 5 days. The resulting solid was filtered off, washed twice with DI and acetone, and dried at 50 °C. Elemental analysis for $MgP_4O_{12}N_2C_{10}H_{26}$ **(2)**: calculated (wt %): C 23.34, H 5.09, N 5.44; found (wt %): C 23.06, H 5.21, N 5.30. Yield ~34% based on the metal.

3.4. Microwave-Assisted Synthesis

The same synthetic conditions used for the scale-up of Compounds **1** and **2** under hydrothermal treatment were established for the microwave-assisted synthesis. The solutions obtained after adjusting the pH were poured into the microwave vials (V_{max} = 30 mL) and heated with stirring at 140 or 180 °C, for Solids **1** and **2**, respectively, and reaction times of 30, 60, and 120 min. The microwave power was fixed in 850 W for all experiments. The resulting solid was filtered off, washed twice with DI and acetone, and dried at 50 °C. Temperature, magnetron power, and pressure were recorded during the whole reaction process.

3.5. Gas Adsorption Characterization

The N_2 adsorption-desorption isotherms for **1** were measured in a Micromeritic ASAP 2020 apparatus (TA Instruments–Waters Cromatografía, S.A, Barcelona, Spain). The sample was degassed under high vacuum, ~5 × 10^{-6} bar, at 220 °C for 12 h. The N_2 isotherms, obtained at 77 K, were analyzed by the Brunauer–Emmett–Teller (BET) method. CO_2 adsorption isotherm for degassed **1** was obtained at 273 K and analyzed by the Dubinin–Radushkevich (DR) method [33].

An amount of 200 mg of each Mg-HDTMP sample studied was placed in contact with ammonia vapors from an aqueous solution of 14 wt % of NH_3 for 5 h in a closed container and then dried with H_2SO_4 for 24 h. Elemental analysis for $MgP_4O_{12}N_2C_{10}H_{26}\cdot(H_2O)_4\cdot(NH_3)_{1.5}$ (**3**): calculated (wt %): C 19.62, H 6.33, N 8.00; found (wt %): C 19.38, H 6.33, N 7.91. Elemental analysis for $MgP_4O_{12}N_2C_{10}H_{26}\cdot(H_2O)_7\cdot(NH_3)_{2.5}$ (**4**): calculated (wt %): C 17.58, H 7.01, N 9.23; found (wt %): C 17.57, H 6.77, N 9.38.

3.6. Structural Characterization

Laboratory X-ray powder diffraction (XRPD) patterns were collected on a PANanalytical X'Pert Pro diffractometer equipped with an X'Celerator detector (PANalytical B.V. Malvern Panalytical B.V., Almelo, The Netherlands). XRPD patterns corresponding to the single phases were auto-indexed using the DICVOL06 program [34], and the space groups were derived from the observed systematic extinctions. The crystal structure of **1** and **2** was successfully solved following an ab initio methodology. The integrated intensities were extracted using the program DAJUST [35], and the crystal structure were solved by direct methods using the program XLENS [36]. For Compound **1**, a starting structural model containing a total of 31 atoms in the asymmetric part of the unit cell was obtained. For Solid **2**, only a partial structural model containing all atoms except the carbon atoms from the alkyl chain, which were localized by difference of Fourier maps, was obtained. Both structural models were optimized by the Rietveld method [37] using the program GSAS [38] and the graphic interface EXPGUI [39]. The following soft constraints were imposed in order to preserve chemically reasonable geometries for the phosphonate, alkyl chain, and amine groups. The soft constrains were/PO_3C tetrahedron/P–O (1.53(1) Å), P–C (1.80(1) Å), O···O (2.55(2) Å), O···C (2.73(2) Å), /$N(CH_2)_3$ amine group/N–C (1.50(1) Å), C···C (2.45(2) Å) and/alkyl chain/C–C (1.50(1) Å), $C_{chain}\cdots C_{chain}$ (2.50(2) Å). No attempts to locate the H atoms were carried out due to the limited quality of the XRPD data. The crystal structure of **1deh** was determined by the Rietveld method [37] using the structure of $MgODTMP\cdot 2H_2O\cdot(DMF)_{0.5}$ as a starting model [12] and soft constraints to maintain chemically reasonable geometries for the phosphonate and the alkyl chain.

Thermodiffractometric data for **1** was obtained for the sample loaded in an Anton HTK 1200N camera (Anton Paar GmbH, Graz, Austria) under static air. Data was collected at different temperature intervals, from room temperature up to 250 °C. A heating rate of 5 °C·min^{-1} and a delay time of 10 min to ensure thermal stabilization were used. The data acquisition range was 4–70° (2θ), with a step size of 0.017° and an equivalent counting time of 230 s per step. Crystallite sizes were calculated using Williamson–Hall plot using HighScore Plus v4.6a software (PANalytical B.V. Malvern Panalytical B.V., Almelo, The Netherlands) and LaB_6 as standard for the determination of the instrumental resolution function.

For Compound **1**, in situ synchrotron powder diffraction data were collected on beamline BL04-MSPD under different pressures of CO_2 (up to ~10 bar) and temperatures at ALBA Synchrotron (Barcelona, Spain). The measurements were carried out in the new ICP-ITQ-ICIQ-ALBA Capillary flow cell (Figure 8), which allows to perform high pressure (up to ~15 bars) and high temperature experiments (up to 750 °C) and/or flow gas(es) during data acquisition and the gas flow, temperature and pressure are remotely controlled with the ITQ-ALBA cabinet. Synchrotron X-ray powder diffraction data was collected using a wavelength of λ = 0.6160 Å selected with a double-crystal Si (111) monochromator. The Debye–Scherrer configuration was used with the sample loaded in a

borosilicate glass capillary with a diameter of 0.7 and a length of 6.7 mm. Patterns were collected over an angular range of 1.7–43° (2θ) and an acquisition time of 100 s.

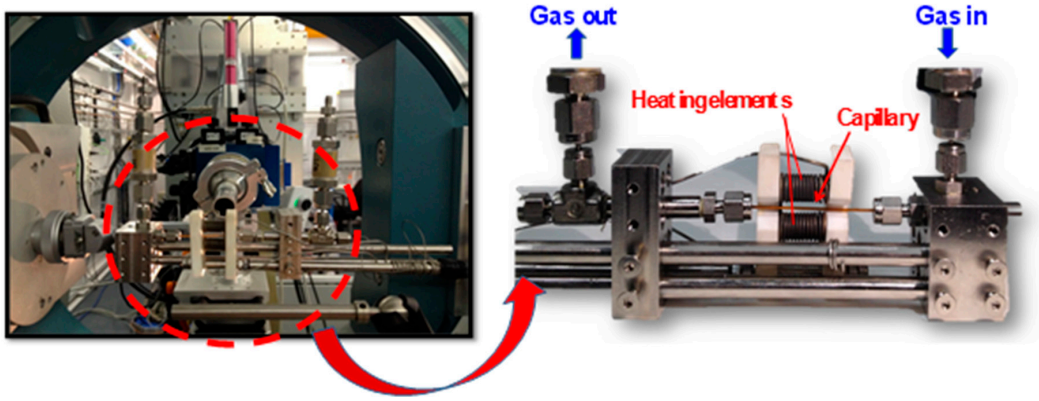

Figure 8. ICP-ITQ-ALBA capillary flow cell installed at the BL04-MSPD beamline, in the powder diffraction station.

3.7. Conductivity Characterization

Impedance measurements were carried out on cylindrical pellets (a diameter of ~5 mm and a thickness of ~1 mm). The pellets were pressed between porous C electrodes (Sigracet, GDL 10 BB, no Pt). The sample cells were placed inside a temperature- and humidity-controlled chamber (Espec SH-222) and connected to an AUTOLAB PGSTAT302N analyzer (Metrohm Autolab B.V., Utrecht, The Netherlands). AC impedance data were collected over the frequency range from 20 to 10^5 Hz with an applied voltage of 0.35 V. To equilibrate water content, pellets were first preheated (0.2 °C/min) from 30 to 80 °C and relative humidity values (RH) of 75 and 95%. Impedance spectra were recorded on cooling using stabilization times of 5 h for each temperature (80, 70, 60, 50, 40, and 30 °C). Water condensation on sample was avoided by reducing first the relative humidity before decreasing temperature. All measurements were electronically controlled by the winDETA package of programs [40].

Supplementary Materials: The following are available online at http://www.mdpi.com/2304-6740/6/3/96/s1, Figure S1. XRPD Rietveld plots for **1**; Figure S2. XRPD Rietveld plots for **1deh**; Figure S3. XRPD Rietveld plots for **2**. Figure S4. *b*-axis view of the H-bond interactions in **1**; Figure S5. N_2 (left) and CO_2 (right) adsorption/desorption isotherms for **1**. Figure S6. Nyquist plots for **1** at (a) 75% and (b) 95% RH; Figure S7. Nyquist plots for **1deh** at (a) 75% and (b) 95% RH; Figure S8. Nyquist plots for **2** at (a) 75% and (b) 95% RH; Figure S9. X-ray powder diffraction patterns for **1** as synthesized and after impedance measurement; Figure S10. X-ray powder diffraction patterns for **2** as synthesized and after impedance measurement; Figure S11. X-ray powder diffraction patterns for **1deh** at 180 °C, after impedance measurements and for **1** for comparative purposes; Table S1. Hydrogen bond distances for **1**; Table S2. Hydrogen bond distances for **1deh**; Table S3. Hydrogen bond distances for **2**. Cif and Cifchecked files. CCDC 1855415, 1855416 and 1855417 contain the supplementary crystallographic data for this paper. These data can be obtained free of charge via http://www.ccdc.cam.ac.uk/conts/retrieving.html (or from the CCDC, 12 Union Road, Cambridge CB2 1EZ, UK; Fax: +44 1223 336033; E-mail: deposit@ccdc.cam.ac.uk).

Author Contributions: R.M.P.C., I.R.S., M.B.-G., E.B., M.P., K.E.P., and D.H.-A.: methodology, investigation, and validation; J.R.: software; P.O.-P., E.R.L., M.A.G.A., K.D.D., and A.C.: funding acquisition, writing (review & editing), and supervision. All authors discussed the results and contributed to the manuscript.

Funding: The work at UMA was funded by the Spanish MINECO project MAT2016-77648-R, which is co-funded by FEDER, and by Junta de Andalucía (Spain) P12-FQM-1656 and FQM-113. The work at UoC was supported by grants from the Research Committee of the University of Crete, ELKE, (Grant # KA 3806).

Acknowledgments: X-ray powder diffraction studies at high CO_2 pressure were performed at MSPD04 beamline (experiment 2012090325) at ALBA Synchrotron with the collaboration of ALBA staff. We also want to thank Prof. Fernando Rey, from the Instituto de Tecnología Química (UPV-CSIC, Valencia, Spain), for his collaboration in the development of the capillary flow cell.

Conflicts of Interest: The authors declare no conflict of interest.

References

1. Clearfield, A.; Demadis, K.D. *Metal Phosphonate Chemistry: From Synthesis to Applications*; Royal Society of Chemistry: Cambridge, UK, 2012; ISBN -13.
2. Moedritzer, K.; Irani, R.R. The Direct Synthesis of α-Aminomethylphosphonic Acids Mannich-Type Reactions with Orthophosphorous. *Acid. J. Org. Chem.* **1966**, *31*, 1603–1607. [CrossRef]
3. Cardiano, P.; Cigala, R.M.; Cordaro, M.; De Stefano, C.; Milea, D.; Sammartano, S. On the complexation of metal cations with "pure" diethylenetriamine-*N*,*N*,*N*′,*N*″,*N*″-pentakis(methylenephosphonic) acid. *New J. Chem.* **2017**, *41*, 4065–4075. [CrossRef]
4. Villemin, D.; Didi, M.A. Aminomethylenephosphonic Acids Syntheses and Applications (A Review). *Orient. J. Chem.* **2015**, *31*, 1–12. [CrossRef]
5. Chirby, D.; Franck, S.; Troutner, D.E. Adsorption of ^{153}Sm-EDTMP on calcium hydroxyapatite. *Int. J. Radiat. Appl. Instrum. Part A* **1988**, *39*, 495–499. [CrossRef]
6. Demadis, K.D.; Barouda, E.; Stavgianoudaki, N.; Zhao, H. Inorganic-Organic Hybrid Molecular "Ribbons" Based on Chelating/Bridging, "Pincer" Tetraphosphonates and Alkaline-Earth Metals. *Cryst. Growth Des.* **2009**, *9*, 1250–1253. [CrossRef]
7. Demadis, K.D.; Mantzaridis, C.; Lykoudis, P. Effects of Structural Differences on Metallic Corrosion Inhibition by Metal−Polyphosphonate Thin Films. *Ind. Eng. Chem. Res.* **2006**, *45*, 7795–7800. [CrossRef]
8. Taddei, M.; Costantino, F.; Ienco, A.; Comotti, A.; Dau, P.V.; Cohen, S.M. Synthesis, breathing, and gas sorption study of the first isoreticular mixed-linker phosphonate based metal–organic frameworks. *Chem. Commun.* **2013**, *49*, 1315–1317. [CrossRef] [PubMed]
9. Colodrero, R.M.P.; Cabeza, A.; Olivera-Pastor, P.; Infantes-Molina, A.; Barouda, E.; Demadis, K.D.; Aranda, M.A.G. "Breathing" in Adsorbate-Responsive Metal Tetraphosphonate Hybrid Materials. *Chem. Eur. J.* **2009**, *15*, 6612–6618. [CrossRef] [PubMed]
10. Colodrero, R.M.P.; Olivera-Pastor, P.; Losilla, E.R.; Aranda, M.A.G.; Papadaki, M.; McKinlay, A.; Morris, R.E.; Demadis, K.D.; Cabeza, A. Multifunctional Lanthanum Tetraphosphonates: Flexible, Ultramicroporous and Proton-Conducting Hybrid Frameworks. *Dalton Trans.* **2012**, *41*, 4045–4051. [CrossRef] [PubMed]
11. Mendes, R.F.; Ananias, D.; Carlos, L.D.; Rocha, J.; Almeida Paz, F.A. Photoluminescent Lanthanide-Organic Framework Based on a Tetraphosphonic Acid Linker. *Cryst. Growth Des.* **2017**, *17*, 5191–5199. [CrossRef]
12. Colodrero, R.M.P.; Olivera-Pastor, P.; Losilla, E.R.; Hernandez-Alonso, D.; Aranda, M.A.G.; Leon-Reina, L.; Rius, J.; Demadis, K.D.; Moreau, B.; Villemin, D.; et al. High Proton Conductivity in a Flexible, Cross-Linked, Ultramicroporous Magnesium Tetraphosphonate Hybrid Framework. *Inorg. Chem.* **2012**, *51*, 7689–7698. [CrossRef] [PubMed]
13. Schütrumpf, A.; Duthie, A.; Lork, E.; Yücesan, G.; Beckmann, J. Synthesis of Some Di- and Tetraphosphonic Acids by Suzuki Cross-Coupling. *Z. Anorg. Allg. Chem.* **2018**, in press. [CrossRef]
14. Feyand, M.; Seidler, C.F.; Deiter, C.; Rothkirch, A.; Lieb, A.; Wark, M.; Stock, N. High-throughput Microwave-assisted Discovery of New Metal Phosphonates. *Dalton Trans.* **2013**, *42*, 8761–8770. [CrossRef] [PubMed]
15. Colodrero, R.M.P.; Angeli, G.K.; Bazaga-Garcia, M.; Olivera-Pastor, P.; Villemin, D.; Losilla, E.R.; Martos, E.Q.; Hix, G.B.; Aranda, M.A.G.; Demadis, K.D.; et al. Structural Variability in Multifunctional Metal Xylenediaminetetraphosphonate Hybrids. *Inorg. Chem.* **2013**, *52*, 8770–8783. [CrossRef] [PubMed]
16. Firmino, A.D.G.; Mendes, R.F.; Antunes, M.M.; Barbosa, P.C.; Vilela, S.M.F.; Valente, A.A.; Figueiredo, F.M.L.; Tomé, J.P.C.; Almeida Paz, F.A. Robust Multifunctional Yttrium-Based Metal−Organic Frameworks with Breathing Effect. *Inorg. Chem.* **2017**, *56*, 1193–1208. [CrossRef] [PubMed]
17. Schütrumpf, A.; Bulut, A.; Hermer, N.; Zorlu, Y.; Kirpi, E.; Stock, N.; Yazaydın, A.O.; Yücesan, G.; Beckmann, J. From Tetrahedral Tetraphosphonic Acids E[*p*-$C_6H_4P(O)(OH)_2]_4$ (E = C, Si) to Porous Cu–and Zn–MOFs with Large Surface Areas. *ChemistrySelect* **2017**, *2*, 3035–3038. [CrossRef]
18. Zaręba, J.K.; Białek, M.J.; Janczak, J.; Nyk, M.; Zoń, J.; Samoć, M. Beyond Single-Wavelength SHG Measurements: Spectrally-Resolved SHG Studies of Tetraphosphonate Ester Coordination Polymers. *Inorg. Chem.* **2015**, *54*, 10568–10575. [CrossRef] [PubMed]

19. Zaręba, J.K. Tetraphenylmethane and tetraphenylsilane as building units of coordination polymers and supramolecular networks—A focus on tetraphosphonates. *Inorg. Chem. Commun.* **2017**, *86*, 172–186. [CrossRef]
20. Rhauderwiek, T.; Wolkersdörfer, K.; Øien-Ødegaard, S.; Lillerud, K.-P.; Wark, M.; Stock, N. Crystalline and permanently porous porphyrin-based metal tetraphosphonates. *Chem. Commun.* **2018**, *54*, 389–392. [CrossRef] [PubMed]
21. Firmino, A.D.G.; Figueira, F.; Tomé, J.P.C.; Almeida Paz, F.A.; Rocha, J. Metal–Organic Frameworks assembled from tetraphosphonic ligands and lanthanides. *Coord. Chem. Rev.* **2018**, *355*, 133–149. [CrossRef]
22. Plabst, M.; McCusker, L.B.; Bein, T. Exceptional Ion-Exchange Selectivity in a Flexible Open Framework Lanthanum(III)tetrakisphosphonate. *J. Am. Chem. Soc.* **2009**, *131*, 18112–18118. [CrossRef] [PubMed]
23. Stock, N.; Rauscher, M.; Bein, T. Inorganic–organic hybrid compounds: Hydrothermal synthesis and characterization of a new three-dimensional metal tetraphosphonate $Mn[(HO_3PCH_2)N(H)(CH_2)_4(H)N(CH_2PO_3H)_2]$. *J. Solid State Chem.* **2004**, *177*, 642–647. [CrossRef]
24. Demadis, K.D.; Mantzaridis, C.; Raptis, R.G.; Mezei, G. Metal–Organotetraphosphonate Inorganic–Organic Hybrids: Crystal Structure and Anticorrosion Effects of Zinc Hexamethylenediaminetetrakis(methylenephosphonate) on Carbon Steels. *Inorg. Chem.* **2005**, *44*, 4469–4471. [CrossRef] [PubMed]
25. Demadis, K.D.; Barouda, E.; Zhao, H.; Raptis, R.G. Structural architectures of charge-assisted, hydrogen-bonded, 2D layered aminetetraphosphonate and zinctetraphosphonate ionic materials. *Polyhedron* **2009**, *28*, 3361–3367. [CrossRef]
26. Mondry, A.; Janicki, R. From structural properties of the Eu^{III} complex with ethylenediaminetetra(methylenephosphonic acid) (H_8EDTMP) towards biomedical applications. *Dalton Trans.* **2006**, *0*, 470–4710. [CrossRef] [PubMed]
27. Wu, J.; Hou, H.; Han, H.; Fan, Y. Highly Selective Ferric Ion Sorption and Exchange by Crystalline Metal Phosphonates Constructed from Tetraphosphonic Acids. *Inorg. Chem.* **2007**, *46*, 7960–7970. [CrossRef] [PubMed]
28. Momma, K.; Izumi, F. VESTA 3 for three-dimensional visualization of crystal, volumetric and morphology data. *J. Appl. Crystallogr.* **2011**, *44*, 1272–1276. [CrossRef]
29. Colomban, P.; Novak, A. Proton Transfer and Superionic Conductivity in Solids and Gels. *J. Mol. Struct.* **1988**, *177*, 277–308. [CrossRef]
30. Villemin, D.; Moreau, B.; Elbilali, A.; Didi, M.-A.; Kaid, M.; Jaffrès, P.-A. Green Synthesis of Poly(aminomethylenephosphonic) Acids. *Phosphorus Sulfur* **2010**, *185*, 2511–2519. [CrossRef]
31. Colodrero, R.M.P.; Olivera-Pastor, P.; Cabeza, A.; Papadaki, M.; Demadis, K.D.; Aranda, M.A.G. Structural Mapping and Framework Interconversions in 1D, 2D, and 3D Divalent Metal R,S-Hydroxyphosphonoacetate Hybrids. *Inorg. Chem.* **2010**, *49*, 761–768. [CrossRef] [PubMed]
32. Colodrero, R.M.P.; Cabeza, A.; Olivera-Pastor, P.; Rius, J.; Choquesillo-Lazarte, D.; García-Ruiz, J.M.; Papadaki, M.; Demadis, K.D.; Aranda, M.A.G. Common Structural Features in Calcium Hydroxyphosphonoacetates. A High-Throughput Screening. *Cryst. Growth Des.* **2011**, *11*, 1713–1722. [CrossRef]
33. Dubinin, M.M.; Radushkevich, L.V. The equation of the Characteristic Curve of Activated Charcoal. *Proc. Acad. Sci. USSR* **1947**, *55*, 331–333.
34. Boultif, A.; Louer, D. Powder pattern indexing with the dichotomy method. *J. Appl. Cryst.* **2004**, *37*, 724–731. [CrossRef]
35. Vallcorba, O.; Rius, J.; Frontera, C.; Peral, I.; Miravitlles, C. DAJUST: A suite of computer programs for pattern matching, space-group determination and intensity extraction from powder diffraction data. *J. Appl. Cryst.* **2012**, *45*, 844–848. [CrossRef]
36. Rius, J. Patterson-function direct methods for structure determination of organic compounds from powder diffraction data. XVI. *Acta Cryst.* **2011**, *A67*, 63–67. [CrossRef] [PubMed]
37. Rietveld, H.M.A. profile refinement method for nuclear and magnetic structures. *J. Appl. Cryst.* **1969**, *2*, 65–71. [CrossRef]
38. Larson, A.C.; Von Dreele, R.B. *General Structure Analysis System (GSAS)*; Los Alamos National Laboratory Report LAUR 86–748; Los Alamos National Laboratory: Los Alamos, NM, USA, 2004.

39. Toby, B.H. EXPGUI, a graphical user interface for GSAS. *J. Appl. Cryst.* **2001**, *34*, 210–213. [CrossRef]
40. *WinDETA*; v 5.66; Novocontrol GmbH: Hundsangen, Germany, 1995.